

Frustrated quantum critical theory of putative spin-liquid phenomenology in 6H-B-Ba₃NiSb₂O₉

G. Chen, M. Hermele, and L. Radzihovsky

Department of Physics, University of Colorado, Boulder, CO 80309, USA

(Dated: November 26, 2018)

A recently discovered material, 6H-B-Ba₃NiSb₂O₉ was found to display unusual low-temperature phenomenology, interpreted as a quantum spin liquid with spin $S = 1$ on a triangular lattice. We study a spin $S = 1$ exchange model on an AB stacked triangular lattice near its quantum paramagnet-to-spiral transition, driven by easy-plane single-ion anisotropy. We demonstrate that the frustrated inter- and intra-layer exchanges induce contour lines of low-energy excitations that lead to a broad crossover regime of linear-temperature dependence of the specific heat. Based on this and various other predictions, we argue that the observed phenomenology can be understood in terms of a conventional picture of a proximity to this frustrated critical point.

PACS numbers: 71.70.Ej, 71.70.Gm, 75.10.-b

Quantum spin liquids (QSLs) are Mott insulators that remain magnetically disordered down to zero temperature, and, as we use term here, are exotic states of matter characterized by properties such as quantum number fractionalization, topological order, and gapless excitations in the absence of spontaneously broken symmetry. The realization of QSLs in theoretical models has been well established[1], and a number of materials have emerged as promising candidates[2–9]. However, there is no direct confirmation of QSL in any of these systems, and alternative explanations now exist for some QSL candidates[10–14].

Many QSL candidates share a rough phenomenology: they are electrical insulators, but with thermodynamic properties similar to those of a metal. In particular, many of these systems have a constant low-temperature spin susceptibility, and a linear-temperature dependence of the low-temperature specific heat. Theoretical attempts to explain this behavior usually invoke spin- $\frac{1}{2}$ fermionic spinons with a constant density of states (DOS). In this Letter, we propose the first (to our knowledge) alternative explanation for this phenomenology that does not invoke substantial quenched disorder.

Recently the compound 6H-B-Ba₃NiSb₂O₉ (6H-B) has been proposed as a QSL candidate[15]. This system has magnetic ions Ni²⁺ forming triangular layers with spin-1 local moments. The Curie-Weiss temperature is -75.5K and no sign of magnetic ordering is detected down to 0.35K , indicating a strong frustration. The system exhibits the QSL phenomenology described above, with a linear- T specific heat and constant spin susceptibility at low temperatures[15]. To account for the experiments, Refs. 16 and 17 proposed QSLs with fermionic spinons. In contrast to these interesting proposals, in this Letter we argue that the 6H-B data can be understood without invoking QSL physics. We propose that the putative QSL behavior arises as a crossover tied to the proximity of a quantum critical point (QCP) between spin spirals favored by the frustrated exchange, and a quantum paramagnetic (QP) phase, favored by a single-ion anisotropy (SIA).

More specifically, in a mean-field treatment we find the dispersion of spin excitations has the schematic form $\epsilon_{\mathbf{k}} = \sqrt{f_1(\mathbf{k})f_2(\mathbf{k})}$. While generically, including at the QCP, there is no special relationship between the functions f_1 and f_2 , in

a broad parameter regime near the QCP f_1 and f_2 are approximately proportional. This leads to an enhanced DOS, and, due to the presence of a degenerate contour of low-energy excitations, a linear intermediate-temperature specific heat. This behavior follows from the form of the dispersion, and is expected to be robust beyond mean-field theory (MFT). The microscopic ingredients for this behavior are SIA combined with comparable Ising and transverse antiferromagnetic exchange. Therefore, we expect that such a deviation from a generic dispersion, accompanied by anomalous intermediate-temperature thermodynamics, should be common in $S > 1/2$ antiferromagnets where the crystal structure admits a SIA. More broadly, there are certainly many mechanisms by which generic behavior may be pushed down to very low temperatures, and the resulting regimes of anomalous intermediate-temperature behavior may be important in various situations, perhaps even in other QSL candidates.

In 6H-B, the Ni triangular layers have an A-B stacking with the lattice sites on one layer projecting to the centers of the triangle plaquettes on the two neighboring layers (Fig. 1). Our minimal model includes the interlayer and intralayer spin exchange and a SIA. Treating the two neighboring triangular layers as the two sublattices of a honeycomb lattice, we view the system as a multilayer honeycomb lattice (Fig. 1). Therefore, when the exchange is dominant and frustrated, the classical ground state is highly degenerate. Quantum fluctuations lift the degeneracy and favor coplanar spiral orders. A strong easy-plane SIA favors a QP state, which is separated from the ordered state by a QCP. We propose that 6H-B is close to this QCP, and may lie either on the QP or magnetically ordered side. The constant spin susceptibility arises from the explicit breaking of spin rotational symmetry by the SIA, and the powder nature of the samples. More notably, we interpret the observed broad linear- T specific heat in terms of the dispersion for spin excitations, as discussed above.

Model—Although the interlayer exchange path goes through one more oxygen than the intralayer coupling, the multiplicity of the former path is larger than the latter. Moreover, in a structurally similar material 6H-A-Ba₃NiSb₂O₉ with long-range magnetic order, the magnetic specific heat at low temperatures is observed to behave as $C_v(T) \sim T^3$,

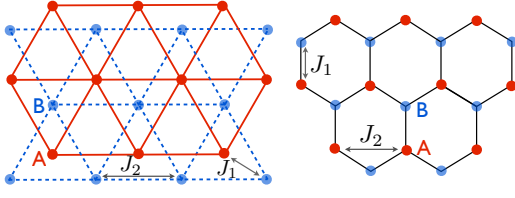


FIG. 1. (Color online) Two adjacent triangular layers of 6H-B (left) can be viewed as a single-layer honeycomb lattice (right). J_1 (J_2) is the interlayer (intralayer) exchange[19]. J_1 is also the exchange between adjacent honeycomb layers.

which indicates a non-negligible interlayer coupling. That may thus be important in understanding the properties of 6H-B, but is not required for our theory. The resulting exchange is given on the triangular multilayers by the Hamiltonian,

$$\mathcal{H}_{\text{ex}} = J_1 \sum_{\langle ij \rangle \in \text{AB}} \mathbf{S}_i \cdot \mathbf{S}_j + J_2 \sum_{\langle ij \rangle \in \text{AA and BB}} \mathbf{S}_i \cdot \mathbf{S}_j. \quad (1)$$

The first sum is for interlayer exchange between nearest-neighbor (NN) sites on neighboring A and B layers, and the second sum is for intralayer exchange between NN sites within the same layer. As illustrated in Fig. 1, the interlayer (intralayer) exchange on a triangular bilayer can be viewed as the nearest-neighbor (next-nearest-neighbor) exchange on a single honeycomb layer. In contrast to Ref. 16, we do not include the biquadratic exchange, which we expect to be strongly subdominant to \mathcal{H}_{ex} .

The space-group symmetry $\text{P6}_3\text{mc}$ of 6H-B restricts the SIA to be $\mathcal{H}_{\text{ani}} = D \sum_i (S_i^z)^2$ with z -axis normal to the triangular layers. Since an easy-axis anisotropy is more likely to favor magnetic order, so we expect easy-plane anisotropy ($D > 0$) for 6H-B, where such order is not observed.

Our model thus contains two competing terms, exchange and SIA, $\mathcal{H} = \mathcal{H}_{\text{ex}} + \mathcal{H}_{\text{ani}}$. Implementing high- T series expansion, we extract the Curie-Weiss temperature, finding that $\Theta_{\text{CW}}^z = -D/3 - 4J$ and $\Theta_{\text{CW}}^\perp = D/6 - 4J$ (where $J \equiv J_1 + J_2$) for field applied along and perpendicular to the z axis, respectively. With a powder sample in experiment[15], a powder average gives $\Theta_{\text{CW}}^{\text{av}} = -4J$ that is independent of D . Furthermore, with Weiss-MFT we demonstrate that saturation temperature of spin susceptibility (observed to be $\sim 25\text{K}$ [15]) is set by D , that is thus comparable to J .

For the Hamiltonian \mathcal{H} , when the SIA dominates with $D \gg J$, the ground state is a uniform QP state with $|S^z = 0\rangle$ at each site. In the opposite limit of dominant exchange, we expect the ground state to be magnetically ordered. Luttinger-Tisza method[20] gives the classical ground state spin configurations with the ordering wavevector $q_z = 0$ and spins lying in the xy plane. When $J_1 > 3J_2$, the classical ground state is a usual Néel state. When $J_1 < 3J_2$, the classical ground state is degenerate with degenerate spiral wavevectors $\mathbf{q}_\perp \equiv (q_x, q_y)$ satisfying $\sum_{\{\mathbf{b}\}} \cos(\mathbf{q}_\perp \cdot \mathbf{b}) = (J_1/J_2)^2 - 3$, where $\{\mathbf{b}\}$ are 6 next-nearest-neighbor lattice vectors of the honeycomb lattice. The degenerate wavevectors form contour

curves in momentum space. Moreover, with vanishing J_1 , this spiral reduces to the familiar 120° state of decoupled triangular layers. Quantum fluctuations lift the degeneracy of these classical spin spirals, selecting states characterized by a discrete set of \mathbf{q} 's around which the quantum zero-point energy is minimized. The spiral ground states favored by the quantum fluctuations do not vary upon introducing the SIA. The optimal spiral wavevectors are given by[18]

$$\mathbf{q}_\perp = \left(0, \frac{2}{\sqrt{3}} \cos^{-1} \left(\left(\frac{J_1}{2J_2} \right)^2 - \frac{5}{4} \right) \right), \quad \text{for } 1 < \frac{J_1}{J_2} < 3 \quad (2)$$

$$\mathbf{q}_\perp = \left(2 \cos^{-1} \left(\frac{J_1}{2J_2} + \frac{1}{2} \right), \frac{2\pi}{\sqrt{3}} \right), \quad \text{for } \frac{J_1}{J_2} < 1, \quad (3)$$

and their symmetry equivalents.

Starting from the magnetically ordered phase, the existence and properties of the phase transition can be analyzed within a Weiss-MFT. We decouple the exchange into an effective Zeeman field which is then self-consistently determined for each sublattice. We parameterize the spin order as,

$$\mathbf{S}_A(\mathbf{r}) = M [\cos(\mathbf{q} \cdot \mathbf{r}) \hat{x} + \sin(\mathbf{q} \cdot \mathbf{r}) \hat{y}], \quad (4)$$

$$\mathbf{S}_B(\mathbf{r}) = M [\cos(\mathbf{q} \cdot \mathbf{r} + \theta) \hat{x} + \sin(\mathbf{q} \cdot \mathbf{r} + \theta) \hat{y}], \quad (5)$$

where θ is the relative phase between two sublattices and depends on J_1/J_2 , and M is the order parameter to be determined. This parameterization describes both the Néel state for $J_1 > 3J_2$ and the spin spirals for $J_1 < 3J_2$, with the 120° state as the limiting case of the decoupled triangular layers. At zero temperature MFT yields that in the vicinity of the QCP the order parameter is $M = \sqrt{2} (1 - \frac{D}{D_c})^{\frac{1}{2}}$ with the critical anisotropy parameter $D_c = 12(J_1 - J_2)$ for the Néel state when $J_1 > 3J_2$, $D_c = 6J_2$ for the 120° state at vanishing J_1 , and $D_c = 6J_2 + \frac{2J_1^2}{J_2}$ for the spin spirals when $J_1 < 3J_2$. We expect that as usual Weiss-MFT overestimates D_c (Fig. 2).

Within Weiss-MFT, in the QP phase, the zero-temperature spin susceptibility $\chi^z = 0$ (fields along z -axis). For fields in xy plane, the spin susceptibility saturates to a constant $\chi_0^\perp = \frac{2\mu_0(g\mu_B)^2}{D+12J}$. The powder average gives the zero-temperature susceptibility $\chi_0^{\text{av}} = 2\chi_0^\perp/3$.

Rotor MFT—It is convenient to model this easy-plane system with rotor variables, by introducing an integer-valued field n_i and 2π -periodic phase variable ϕ_i , which satisfy $[\phi_i, n_j] = i\delta_{ij}$. With the mapping ($S_i^z \rightarrow n_i$, $S_i^\pm \rightarrow \sqrt{2}e^{i\phi_i}$), the rotor Hamiltonian reads

$$\mathcal{H}_{\text{rotor}} = \sum_{ij} J_{ij} [\cos(\phi_i - \phi_j) + n_i n_j / 2] + \sum_i D n_i^2, \quad (6)$$

where J_{ij} takes J_1 (J_2) for NN interlayer (intralayer) bonds. Although n_i only takes the values of $\pm 1, 0$ in the spin model, due to the substantial anisotropy D , we expect that relaxing this restriction is unlikely to have significant effects.

Using the coherent-state path integral, we integrate out the field n_i and obtain the partition function,

$$\mathcal{Z} = \int \mathcal{D}\Phi \mathcal{D}\lambda e^{-S - i \sum_i \int d\tau \lambda_i (|\Phi_i|^2 - 1)}, \quad (7)$$

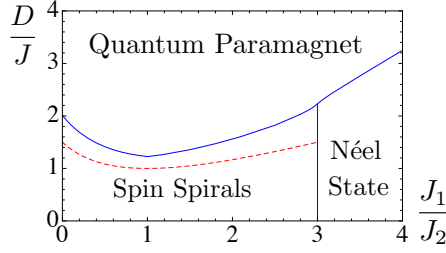


FIG. 2. Zero-temperature phase diagram determined from the SPE. Dashed curve indicates the location where $D = \Delta_0/2$, which is important in the discussion of T -linear $C_v(T)$ below.

where $\mathcal{S} = \int d\tau \sum_{\mathbf{k}} (4D\mathbb{I} + 2\mathcal{J}_{\mathbf{k}})^{-1} \partial_{\tau} \Phi_{\mu,\mathbf{k}}^* \partial_{\tau} \Phi_{\nu,-\mathbf{k}} + \sum_{ij} J_{ij} \Phi_i^* \Phi_j$ with $\Phi_i^* \equiv e^{i\phi_i}$. $\mathcal{J}_{\mathbf{k}}$ is the 2×2 exchange coupling matrix in momentum space, μ, ν are the sublattice indices, and \mathbb{I} is a 2×2 identity matrix. The constraint $|\Phi_i| = 1$ is enforced by the Lagrange multiplier λ_i . We proceed by a saddle-point approximation. Assuming $i\lambda_i = \beta\Delta(T)$ at the saddle point, we integrate out the Φ field and obtain the saddle-point equation (SPE) for $\Delta(T)$ in paramagnetic phase,

$$\sum_{i=\pm} \int_{\mathbf{k} \in \text{BZ}} \frac{d^3\mathbf{k}}{u_{\text{BZ}}} \frac{2D + s_{i,\mathbf{k}}}{\epsilon_{i,\mathbf{k}}} \coth\left(\frac{\beta\epsilon_{i,\mathbf{k}}}{2}\right) = 2, \quad (8)$$

where $u_{\text{BZ}} = \frac{16\pi^3}{\sqrt{3}}$ is the Brillouin zone (BZ) volume, $s_{\pm,\mathbf{k}} \equiv J_2 \sum_{\{\mathbf{b}\}} \cos(\mathbf{k} \cdot \mathbf{b}) \pm 2|J_1 \cos(\frac{k_x}{2})| \sqrt{3 + \sum_{\{\mathbf{b}\}} \cos(\mathbf{k} \cdot \mathbf{b})}$ are the eigenvalues of $\mathcal{J}_{\mathbf{k}}$, and $\epsilon_{\pm,\mathbf{k}}$ are the two spin excitations,

$$\begin{aligned} \epsilon_{\pm,\mathbf{k}} &= \sqrt{(4D + 2s_{\pm,\mathbf{k}})(\Delta(T) + s_{\pm,\mathbf{k}})} \\ &= \sqrt{2[(s_{\pm,\mathbf{k}} + D + \frac{\Delta(T)}{2})^2 - (D - \frac{\Delta(T)}{2})^2]}. \end{aligned} \quad (9)$$

When the left-hand side of the SPE is less than 2 for any $\Delta(T)$, the rotor is condensed which signals magnetic ordering. Therefore, besides the transition temperature from the high-temperature paramagnetic phase to the low-temperature spin spirals, we also obtain the critical D_c that separates spin spirals from QP phase and the zero-temperature phase diagram (Fig. 2). As expected, D_c obtained here is smaller than the one determined previously from the Weiss-MFT. In particular, D_c/J is minimal at $J_1 = J_2$ corresponding to the largest frustration at this point. Right at the QCP and zero temperature, $\Delta(0) \equiv \Delta_0 = 3J_2 + J_1^2/J_2$ and the low-energy mode $\epsilon_{-, \mathbf{k}}$ develops gapless excitations. As shown in Fig. 3, the momenta of the gapless excitations form contour lines that are identical to the ones of degenerate classical ground state spiral wavevectors. Moreover, as J_1/J_2 increases from 0, the contour lines around the BZ corners gradually expand and meet at M when $J_1 = J_2$.

Near the QCP with $T \ll J - \Delta(T)$ increases with T and we define $\Delta(T) \equiv \Delta_0 + \Delta_1(T)$. The excitation $\epsilon_{\pm}(\mathbf{k})$ picks up a self-energy via the T -dependence of $\Delta(T)$. By numerically solving the SPE, we find that, near the QCP

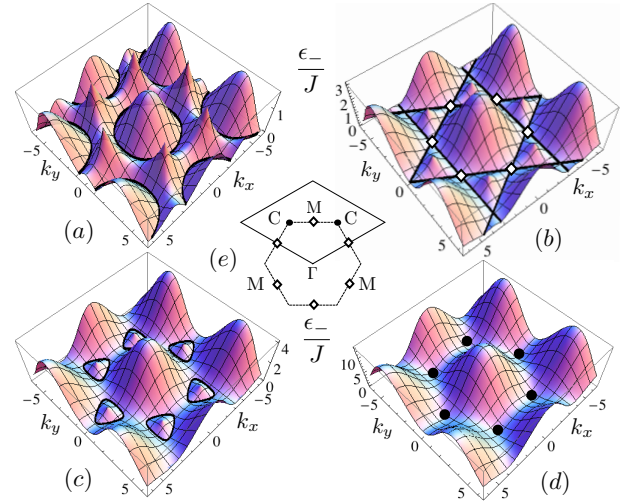


FIG. 3. (Color online) The evolution of the low-energy excitations in k_x - k_y plane with $k_z = 0$ at the QCP. The parameters used in the figures are (a) $J_1 = 1.5J_2$, $D_c = 1.36J$, (b) $J_1 = J_2$, $D_c = 1.23J$, (c) $J_1 = 0.8J_2$, $D_c = 1.28J$, (d) $J_1 = 0$, $D_c = 2.01J$. The low-energy gapless contours are marked with bold black lines in (a-c), while in (d) the low-energy gapless points are marked with black dots. Lattice constants are set to 1. (e) is the BZ of a honeycomb lattice. For $J_1 > J_2$, the contour line is centered in the middle of BZ. For $J_1 < J_2$, the contour lines are centered around and eventually shrink to the corners of BZ in the limit $J_1 \rightarrow 0$. The “ \diamond ” in (b) correspond to M in (e).

$\Delta_1(T) \propto T^2$ for $T \ll J$. This is also supported by an analytical argument (Supplemental Material[19]), and holds in the quasi-2D limit $J_1 \ll J_2$. This immediately leads to the internal energy $E \propto T^3$ and hence $C_v \propto T^2$, for $T \ll \Omega$ with Ω an energy cutoff. This low-temperature T^2 - C_v regime is confirmed numerically in Fig. 4(a).

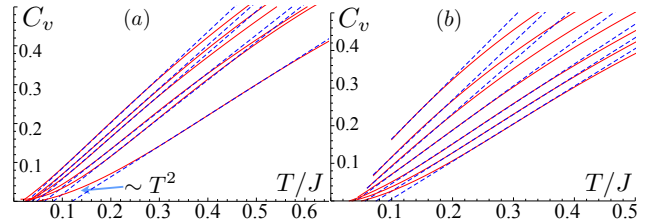


FIG. 4. (Color online) The C_v - T plots in the paramagnetic phase. In (a), from top to bottom, $J_1 = J_2, 0.7J_2, 1.5J_2, 1.8J_2, 0.3J_2, 0$ with $D \approx D_c$ and $D = 1.24J, 1.31J, 1.36J, 1.47J, 1.58J, 2.01J$, respectively. In (b), $J_1 = 0.5J_2$, $D = 1.08J, 1.17J, 1.23J, 1.32J, 1.41J, 1.48J, 1.55J$ from top to bottom. For $D = 1.08J, 1.17J, 1.23J, 1.32J$, $T_c = 0.10J, 0.07J, 0.064J, 0.04J$, respectively. For $J_1 = 0.5J_2$, $D_c = 1.41J$. The dashed lines are the linear fits for a range of data points. Energy is in units of J .

In Fig. 4(a), we also find that, as J_1/J_2 moves to the point $J_1 = J_2$ from either side, the temperature range of the T^2 - C_v regime diminishes. We attribute this to the observation that the zero-temperature DOS at the QCP increases with energy, then saturates to a roughly constant value. This saturation energy

(in units of J) is found to be lowest when $J_1 = J_2$.

Linear- T C_v at intermediate T —In Fig. 4, we find an intermediate-temperature regime with $C_v \approx c_1 T + c_0$. To explain this, we first note that when $D \approx \frac{\Delta(T)}{2}$, the low-energy excitation is approximately the square root of a perfect square:

$$\begin{aligned} \epsilon_{-,k} &\approx \sqrt{2}|s_{-,k} + D + \Delta(T)/2| \\ &\approx \sqrt{2}\left(D + \frac{\Delta_1(T) - \Delta_0}{2}\right) + \frac{k_{\perp}^2}{2m_{\perp,k_0}} + \frac{k_z^2}{2m_{z,k_0}} \end{aligned} \quad (10)$$

If $D = \frac{\Delta_0}{2}$, such dispersion on contour lines in 3D gives a constant DOS at low energies and, because $\Delta(T)$ is only weakly T -dependent in this case, this leads to $C_v \propto T$ at low T . This conclusion also holds in the 2D limit $J_1 \ll J_2$. As shown in Fig. 2, D_c is slightly greater than $\frac{\Delta_0}{2}$ and the system at $D = \frac{\Delta_0}{2}$ is ordered at very low T . Once the system enters into the paramagnetic phase, a linear- T C_v is obtained (see the top curve in Fig. 4(b)). Moreover, this linear- T C_v regime persists even when D is increased to or slightly beyond D_c .

Discussion—The spin susceptibility is observed to saturate to a constant below 25K[15], which is consistent with our prediction. Experiments also find $C_v(T) \simeq \gamma T^\eta$ with $\eta \approx 1.0$ (1) for $0.35\text{K} < T < 7\text{K}$. Determination of both behaviors relies on subtracting a magnetic impurity contribution, which has a significant effect below about 25K and 1K for χ and C_v , respectively. The subtraction procedure for C_v relies on fitting $C_v(T, B = 0\text{T}) - C_v(T, B = 9\text{T})$ to a Schottky form appropriate for a magnetic impurity contribution. This procedure may be unreliable, because 9T is a large field scale for 6H-B, corresponding in temperature units to $\sim 20\text{K}$, and the fitted difference of C_v is thus expected to include a significant contribution from bulk Ni moments. While this complicates interpretation of the $C_v(T)$ for $T \lesssim 1\text{K}$, we note that $C_v(T)$ is certainly linear for $1\text{K} < T < 7\text{K}$ (or $0.05J < T < 0.34J$).

As illustrated in Fig. 4 for some parameter values, the range of the linear- T specific heat of the experiments is compatible with our results for a range of J_1/J_2 [15]. Taking $J_1 = 0.5J_2$ and $D = 1.32J$ (Fig. 4(b)), we find the powder-averaged zero-temperature spin susceptibility $\chi_0^{\text{av}} \approx 0.0124\text{emu/mol}$, which is very close to the experimental value 0.013emu/mol . Moreover, the coefficient γ in $C_v(T)$ is found to be 204mJ/mol-K^2 while the experimental value is 168mJ/mol-K^2 . We obtain a Wilson ratio of 4.4, not far from the experimental value 5.6. The agreement can be further improved by adjusting J_1/J_2 and D .

6H-B may lie either on the QP or magnetically ordered side of the QCP. At very low temperatures we thus expect either

a small energy gap, or the onset of spin order. It should be noted that the presence of magnetic impurities may interfere with observation of such very-low- T behavior. To detect the energy gap or spiral order, NMR or μSR measurements may be helpful. If 6H-B is in the QP phase, then in a single crystal sample we predict $\chi^z = 0$, $\chi^\perp = \text{const}$ at zero temperature. Ref. 16 considered a state with gapped $S^z = \pm 1$ fermions and gapless $S^z = 0$ fermions forming a Fermi surface. This state has a spin gap, with thermodynamic properties dominated by the Fermi surface. The two QSLs in Ref. 17 have gapless spin excitations. These states are thus distinct from the QP phase of our proposal, which has a fully gapped spectrum. Especially if single crystal samples are available, inelastic neutron scattering should be able to further distinguish these proposals by measuring the dispersion of low-energy spin excitations; our prediction is depicted in Fig. 3.

To summarize, we propose a minimal J_1 - J_2 - D model for 6H-B and argue that its putative QSL phenomenology is due to the proximity to a QCP. Our theoretical prediction is broadly compatible with current experiments[15]. Various future experimental directions are suggested.

Acknowledgement— We thank L. Balicas, P. Lee and L. Thompson for discussion. This research is supported by David and Lucile Packard Foundation (G.C. and M.H.) and NSF through grant no. DMR-1001240 (G.C. and L.R.).

-
- [1] L. Balents, *Nature* **464**, 199 (2010).
 - [2] J. Gardner *et al*, *Phys. Rev. Lett.* **82**, 1012 (1999).
 - [3] Z. Hiroi *et al*, *J. Phys. Soc. Jpn.* **70**, 3377 (2001).
 - [4] Y. Shimizu *et al*, *Phys. Rev. Lett.* **91**, 107001 (2003).
 - [5] J. S. Helton *et al*, *Phys. Rev. Lett.* **98**, 107204 (2007).
 - [6] Y. Okamoto *et al*, *Phys. Rev. Lett.* **99**, 137207 (2007).
 - [7] T. Itou *et al*, *Phys. Rev. B* **77**, 104413 (2008).
 - [8] Y. Okamoto *et al*, *J. Phys. Soc. Jpn.* **78**, 033701 (2009).
 - [9] M. de Vries *et al*, *Phys. Rev. Lett.* **104**, 177202 (2010).
 - [10] M. Kohno *et al*, *Nature Physics* **3**, 790 (2007).
 - [11] O. A. Starykh *et al*, *Phys. Rev. B* **82**, 014421 (2010).
 - [12] E. Stoudenmire *et al*, *Phys. Rev. B* **79**, 214436 (2009).
 - [13] G. Chen *et al*, *Phys. Rev. Lett.* **102**, 096406 (2009), G. Chen *et al*, *Phys. Rev. B* **80**, 224409 (2009).
 - [14] R. R. P. Singh, *Phys. Rev. Lett.* **104**, 177203 (2010).
 - [15] J. Cheng *et al*, *Phys. Rev. Lett.* **107**, 197204 (2011).
 - [16] M. Serbyn *et al*, *Phys. Rev. B* **84**, 180403 (2011).
 - [17] C. Xu *et al*, *Phys. Rev. Lett.* **108**, 087204 (2012).
 - [18] A. Mulder *et al*, *Phys. Rev. B* **81**, 214419 (2010).
 - [19] See Supplemental Material for the interlayer couplings in 3D.
 - [20] J. M. Luttinger and L. Tisza, *Phys. Rev.* **70**, 954964 (1946).

SUPPLEMENTARY MATERIAL

Here we provide a detailed analytical argument for the T^2 specific heat at low temperature near the QCP. At finite temperature, $\Delta(T)$ increases with temperature and we define $\Delta(T) \equiv \Delta_0 + \Delta_1(T)$. The spin excitation $\epsilon_{\pm}(\mathbf{k})$ also picks up a self-energy via

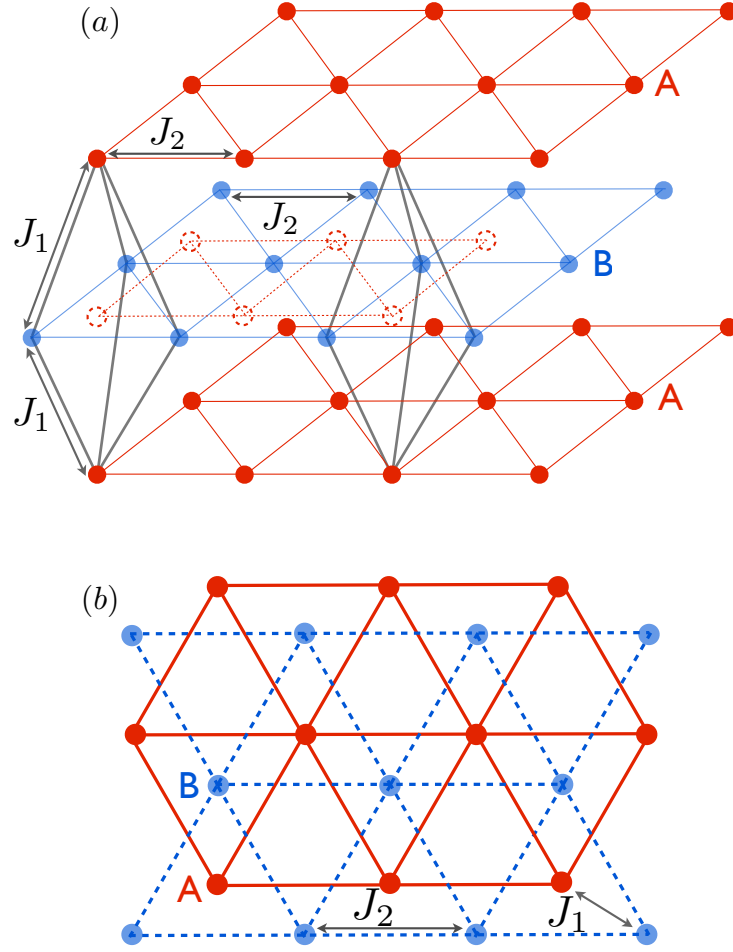


FIG. 5. (Color online) The couplings in the multilayer triangular structure of 6H-B-Ba₃NiSb₂O₉. J_1, J_2 are the interlayer and intralayer couplings, respectively. (a) is the three dimensional view of the lattice structure. The dashed circles on the B plane are the projected positions of the lattice sites from the A plane. (b) is the top view of the lattice (also shown in the main text).

the temperature dependence of $\Delta(T)$. By numerically solving the saddle-point equation, we find that, near the QCP $\Delta_1(T) \propto T^2$ at $T \ll J$. At $T \ll J$, the low-energy spin excitation near the contour lines can be approximated as,

$$\epsilon_{-, \mathbf{k}} \approx \sqrt{A\Delta_1(T) + v_{\perp, k_0}^2 k_{\perp}^2 + v_{z, k_0}^2 k_z^2}, \quad (11)$$

where $A = 4D_c - 2\Delta_0$, k_0 is a momentum coordinate running along the contour lines, k_{\perp} is normal to the tangent of the contour line at k_0 , and we have neglected the weak temperature dependence of the speeds v_{\perp}^2, v_z^2 . Eq. (11) is expected to be a good approximation for $\epsilon_{-}(\mathbf{k})$ less than a cutoff energy Ω with $T \ll \Omega \ll J$. The saddle-point equation can be approximated as

$$\int_{k_0, k_{\perp}, k_z}^{\Lambda} \frac{A \coth(\frac{\beta}{2} \sqrt{A\Delta_1 + v_{\perp}^2 k_{\perp}^2 + v_z^2 k_z^2})}{2\sqrt{A\Delta_1 + v_{\perp}^2 k_{\perp}^2 + v_z^2 k_z^2}} + b = 2, \quad (12)$$

where the integral is over the region around the contour lines with $|k_{\perp}|, |k_z| \lesssim \Lambda$, and b is the approximately T -independent contribution from outside this region. At low temperature, the temperature-dependent part of the integral becomes independent of the cutoff Ω , and only depends on T via the dimensionless parameter $\frac{A\Delta_1(T)}{T^2}$. In order for the integral to be constant in temperature, we thus expect $\Delta_1(T) \propto T^2$ in the limit $T \ll \Omega$. This result immediately leads to the internal energy, which can be approximated as

$$E \sim \int_{k_0, k_{\perp}, k_z}^{\Lambda} \frac{\sqrt{A\Delta_1(T) + v_{\perp}^2 k_{\perp}^2 + v_z^2 k_z^2}}{e^{\beta \sqrt{A\Delta_1(T) + v_{\perp}^2 k_{\perp}^2 + v_z^2 k_z^2}} - 1} \propto T^3 \quad (13)$$

for $T \ll \Omega$. This gives $C_v \propto T^2$ in this temperature regime.